OPEN

Lipocalin-2 Is Induced by Uromodulin Aggregates without Affecting Kidney Disease Progression in Autosomal Dominant Tubulointerstitial Kidney Disease–*UMOD*

Jennifer Lake[1,2] *Marta Mariniello*[1] *Guglielmo Schiano*[1] *Qin Guo*[1] *Holly Mabillard*[3] *John A. Sayer*[3,4,5] *Eric Olinger*[6] *Fabiola Terzi*[2] *and Olivier Devuyst*[1,7]

Key Points

- Lipocalin-2 upregulation paralleled intracellular uromodulin aggregates in mouse and cellular models of autosomal dominant tubulointerstitial kidney disease because of pathogenic uromodulin.
- The induction of lipocalin-2 was triggered by mutant uromodulin accumulation and endoplasmic reticulum stress in tubular cells.
- Genetic loss of lipocalin-2 reduced iron deposits in the kidney but did not affect kidney damage, indicating that lipocalin-2 was not driving disease progression.

Abstract

Background Autosomal dominant tubulointerstitial kidney disease due to pathogenic *UMOD* variants (ADTKD-*UMOD*) is a toxic proteinopathy caused by intracellular accumulation of mutant uromodulin (UMOD) and endoplasmic reticulum (ER) stress. Lipocalin-2 (LCN2) is an acute phase protein induced by ER stress with context-dependent roles in kidney injury.

Methods To examine the role of LCN2 in ADTKD-*UMOD*, we used *Umod* knock-in mouse models (C171Y, R186S, C125R), urine samples from affected patients, and mIMCD3 cells expressing wild-type or mutant UMOD. LCN2 expression was assessed by immunoblotting, immunostaining, and ELISA. Autophagy was stimulated with Torin1 to evaluate effects on LCN2 induction. $Umod^{R186S/+}$ mice were crossed with $Lcn2^{-/-}$ mice to determine the impact of LCN2 deficiency on disease progression.

Results Robust LCN2 induction was observed in kidneys and urine of $Umod^{R186S/+}$, $Umod^{C125R/+}$, and $Umod^{C171Y/+}$ mice, correlating with UMOD aggregates and ER stress severity in thick ascending limb cells. In patients, specific *UMOD* variants were associated with elevated urinary LCN2. In mIMCD3 cells expressing mutant UMOD (C170Y, R185S), treatment with Torin1 reduced aggregates and attenuated LCN2 induction. Genetic deletion of *Lcn2* in $Umod^{R186S/+}$ mice decreased interstitial iron deposition but did not alter UMOD accumulation, interstitial inflammation, or fibrosis.

Conclusions LCN2 was induced by intracellular UMOD aggregates and ER stress in various models of ADTKD-*UMOD*. Although it influenced iron handling, LCN2 did not drive fibrosis or inflammation, supporting a role as a biomarker of toxic proteinopathy rather than a therapeutic target.

JASN 00: 1–15, 2026. doi: https://doi.org/10.1681/ASN.0000001077

[1]Mechanisms of Inherited Kidney Disorders Group, Institute of Physiology, University of Zurich, Zurich, Switzerland
[2]Université de Paris Cité, INSERM U1151, CNRS UMR 8253, Institut Necker Enfants Malades, Paris, France
[3]Newcastle University, Translational and Clinical Research Institute, Newcastle upon Tyne, United Kingdom
[4]Renal Services, The Newcastle upon Tyne Hospitals NHS Foundation Trust, Newcastle, United Kingdom
[5]Newcastle Biomedical Research Centre, Newcastle University, Newcastle, United Kingdom
[6]Center for Human Genetics, Cliniques universitaires Saint-Luc, Brussels, Belgium
[7]Institute for Rare Diseases, Cliniques universitaires Saint-Luc, UCLouvain, Brussels, Belgium

Correspondence: Dr. Olivier Devuyst, email: olivier.devuyst@uzh.ch

Received: November 28, 2025 **Accepted:** March 17, 2026
Published Online Ahead of Print: March 26, 2026

J.L. and M.M. contributed equally to this work.

Introduction

Missense variants in *UMOD* cause autosomal dominant tubulointerstitial kidney disease (ADTKD-*UMOD*), one of the most common monogenic kidney diseases.[1,2] ADTKD-*UMOD* is characterized by tubular damage and interstitial fibrosis, eventually causing kidney failure in young adults. To date, there is no treatment available to slow the progression of ADTKD-*UMOD*.[1] *UMOD* encodes for uromodulin (UMOD), a kidney-specific protein essentially produced by the cells lining the thick ascending limb (TAL) of the loop of Henle. UMOD performs multiple physiological roles in tubular cells and the lumen, including regulation of NaCl transport, protection against urinary tract infections, and inhibition of kidney stone formation.[3]

Key features of ADTKD-*UMOD* include accumulation of mutant UMOD in the endoplasmic reticulum (ER) of the TAL cells, reflected by lower UMOD levels in the urine.[4] *In vitro* studies confirmed altered trafficking, ER retention, and reduced apical release of mutant UMOD,[5] whereas mouse models carrying *Umod* pathogenic variants recapitulated UMOD accumulation in TAL cells, activation of ER stress pathways, and tubulointerstitial damage and kidney fibrosis.[6–10] The recent characterization of three *Umod* knock-in (KI) mouse lines carrying human variants (p.C126R, p.C170Y, and p.R185S) recapitulated the variable disease progression observed in corresponding patients with ADTKD-*UMOD*, with strong allelic and gene dosage effects.[10,11] Disease progression was driven by accumulation of intracellular UMOD aggregates, triggering adaptive or deleterious pathways. *Lcn2*, the gene coding for lipocalin-2 (LCN2), was the most significantly upregulated gene in kidneys of the $Umod^{R186S}$ mice characterized by a severe, early onset of disease, with abundant UMOD aggregates driving inflammation and fibrosis.[11]

LCN2, also known as neutrophil gelatinase–associated lipocalin (NGAL), is a 25 kDa glycoprotein expressed in various cell types, including kidney tubular cells.[12] LCN2 behaves as an acute phase protein, induced in stress situations including inflammation, infection, ischemic damage, and cancer.[13] Through an eight-stranded, antiparallel β-barrel, LCN2 binds to bacterial siderophores, providing innate defense against iron-dependent bacteria.[14] LCN2 also binds endogenous siderophores in humans,[15] with a capacity to modulate intracellular iron concentrations and to play a role in iron homeostasis.[16] Studies using *Lcn2* knock-out mice showed that LCN2 has the capacity to amplify the NF-κB pathway to induce proinflammatory cytokines.[17]

In the basal state, low levels of circulating LCN2 are filtered and reabsorbed by the proximal tubule cells. In case of AKI, LCN2 is strongly induced in distal tubular segments, driving increased levels in blood and urine.[18] These features explain the potential value of LCN2/NGAL as a biomarker for AKI and for monitoring CKD.[19] Beyond a biomarker, LCN2 may also exert beneficial or detrimental roles in different types of kidney disease or injury. For example, administration of LCN2 was shown to decrease apoptosis and tubular damage in a mouse model of ischemia-reperfusion injury.[20,21] Conversely, LCN2 was instrumental for disease progression in a mouse model of nephron reduction and in a mouse model of proteinuria.[22,23]

In this study, we leveraged mouse models, cellular systems, and patient-derived samples to investigate the mechanisms underlying LCN2 induction in ADTKD-*UMOD* and to explore its potential contribution to disease progression.

Methods

See the Supplemental Methods for detailed information.

Sex as a Biological Variable

Both male and female mice were included in all experimental groups to account for potential sex-related differences in disease manifestation. In previous analyses using $Umod^{R186S/+}$ and $Umod^{C171Y/+}$ models, sex-stratified data did not reveal any major effect of sex on disease progression across genotypes.[11] Consistently, no significant sex-related differences were observed here in UMOD accumulation, LCN2 induction, or histopathological outcomes. Data from both sexes were therefore pooled for analysis, except for genes involved in iron metabolism, for which expression values were normalized to account for sex-related differences. In the human cohort, both male and female patients with ADTKD-*UMOD* were included, and urinary LCN2 levels were analyzed independently of sex, with no significant differences detected.

Mouse Models

Three KI mouse lines bearing human ADTKD-*UMOD* variants were used: $Umod^{R186S}$ and $Umod^{C171Y}$ mice (C57BL/6N background); $Umod^{C125R}$ (C57BL/6J background); and the $Lcn2^{+/-}$ mice (C57BL/6J background), to be crossed with the $Umod^{R186S/+}$ mice.[10,11,24] For all studies, littermate animals of both sexes were used. Controls were appropriate littermates for each genotype.

Animals, Housing, and Ethical Considerations

Animals were housed in a temperature-controlled and humidity-controlled pathogen-free facility with free access to acidified water and fed *ad libitum*. Cages included environmental enrichment (nesting material and shelters). To minimize confounders, animals directly compared within each analysis were housed in the same room, and metabolic cage experiments were performed in the same room with the same setup according to standard operating procedure. Different lines could originate from different rooms, but only animals from the same room were compared. Procedures were performed using standardized protocols by the same operator or a small consistent set of operators. No surgical or invasive procedures were performed, and animals were handled only as needed for genotyping and phenotyping. Animals were monitored regularly for general health, including body condition, activity, grooming, and appearance. Humane end points were defined *a priori*; no animals reached these end points. Minor health issues unrelated to the study (*e.g.*, overgrown teeth) were managed according to institutional guidelines, and no adverse events related to experimental procedures were observed.

Cell Models

Immortalized mouse inner medullary collecting duct (mIMCD-3, American Type Culture Collection CRL-2123) cells were transduced with lentiviral particles for the expression of the indicated GFP-tagged human *UMOD* isoforms (wild-type [WT], C170Y and R185S) as reported previously.[11,25]

Human Samples

Clinical and genetic information for patients with ADTKD-*UMOD* with available urine samples (n=23) were provided from clinical partners from Newcastle University. The collection of clinical data was undertaken with informed consent, and ethical approval was given by the National Research Ethics Service Committee North East—Newcastle and North Tyneside 1 and the National Research Ethics Service Committee North East. Control urine samples (n=31), matched for age and sex, were retrieved from a population-based study involving people of European descent aged 35–75 years from the city of Lausanne, Switzerland. The study was approved by the Ethics Committee of the Canton of Vaud, and all participants gave written informed consent.[25]

Biochemical Analysis and Tissue Collection

Plasma and urine levels of creatinine, electrolytes, uric acid, and urea were measured on UniCel DxC 800 Synchron Clinical System or AU480 Clinical Chemistry System (Beckman Coulter, Brea, CA). Urine and plasma osmolality were measured on a multisample osmometer (Advanced Instruments Osmometer 2020, Norwood, MA). Urinary levels of LCN2 were measured with a Mouse ELISA Kit (Thermo Fischer Scientific, #EMLCN2) and normalized on urinary creatinine. After the collection of plasma samples, kidneys were decapsulated, one kidney was flash frozen for RNA extraction, and the other was processed for protein extraction (half) and histological analyses (half). Levels of LCN2 were measured in urine of patients with ADTKD and healthy controls with a Human LCN2/NGAL ELISA Kit #DLCN20 (R&D systems, Minneapolis, MN).

Protein Samples Preparation and Immunoblotting

Protein samples were prepared as previously described.[11] Kidney tissue and cells were lysed in radioimmunoprecipitation assay buffer (Sigma–Aldrich, St.-Louis, MO) supplemented with protease inhibitors (1836153001, Roche, Basel, Switzerland) and phosphatase inhibitors (04906845001, Sigma–Aldrich) using an IKA T10 basic tissue homogenizer (IKA, Staufen, Germany) or cell scraper (99002, TPP Techno Plastic Products, Trasadingen, Switzerland). Lysates were sonicated (amplitude 40%, 1 second, twice) and centrifuged 15 minutes, 1000 g at 4°C to remove debris. Protein lysates were diluted in Laemmli sample buffer (Bio-Rad, Hercules, CA) and dithiothreitol (except for UMOD), boiled 5 minutes at 95°C, and loaded. Proteins were separated on sodium dodecyl sulfate–polyacrylamide gel electrophoresis gel and blotted onto polyvinylidene fluoride or nitrocellulose membranes. Membranes were blocked in 5% w/v nonfat dry milk solution and incubated with primary antibodies. Membranes were incubated with peroxidase-conjugated secondary antibodies and visualized by Immobilon Western horseradish peroxidase Substrate (Millipore, Burlington, MA). Immunoblots were quantified by densitometry using Image Lab.

RNA Isolation, Reverse Transcription, and Quantitative PCR

Total RNA was extracted as previously described from kidney using Aurum™ Total RNA Fatty and Fibrous Tissue Kit (7326830, Bio-Rad, Hercules, CA) and from cells using Direct-zol RNA MiniPrep Plus (R2072, Zymo Research, Irvine, CA).[11] Reverse transcriptase reaction with iScript™ cDNA Synthesis Kit (Bio-Rad) was executed with up to 1 μg of RNA. RT-qPCR was performed with a CFX96™ Real-Time PCR Detection System and the iQ SYBR Green Supermix (Bio-Rad). Normalization was performed using housekeeping genes (*Gapdh*, *Hprt1)*. The relative changes were determined by the formula: $2^{-\Delta\Delta ct}$ and expressed as fold change relative to $Umod^{+/+}$. The list of primers can be found in Supplemental Table 3.

RNA-Sequencing and Bioinformatic Analysis

Volcano plots were generated with GraphPad Prism using previously described RNA-seq data.[11] Heat maps were generated using ExpressAnalyst.[26] Primary RNA-sequencing data are available on Gene Expression Omnibus (accession number: GSE214491).

Histological Analysis and Immunostaining

Mouse kidneys were harvested and processed as previously.[11] For immunofluorescence analysis, kidney sections were incubated with the primary antibody for 2 hours (kidney) or overnight (kidney and cells). The sections were next incubated with the appropriate secondary antibody (AlexaFluor-conjugated, 1:300 [kidney], 1:400 [cells], Life Technologies, Carlsbad, CA). The sections were counterstained with 4′,6-diamidino-2-phenylindole. The slides were imaged with a confocal microscope (Leica Microsystems GmbH, Wetzlar, Germany) using a 63× 1.4 NA oil immersion objective. Staining of kidney sections using Picrosirius Red staining, Perls Prussian blue reaction, or immunohistochemical staining combined with Pearls Prussian blue were evaluated. For semiquantitative analysis, similarly to our previously described method, full kidneys were acquired at a resolution of 20× by a Zeiss Axio Scan.z1 slide scanner (Carl Zeiss, Oberkochen, Germany), equipped with a Hitachi HV-F202FCL digital video camera (Hitachi, Tokyo, Japan).[11]

Cell Culture and Treatments

For autophagy activation, cells were treated with 250 nM of the mTORC1 inhibitor Torin1 (4247; Tocris Bioscience, Bristol, UK) for 16 hours, followed by analysis by Western blot. For ER stress induction, cells were treated with 0.3 μM of the SERCA pump inhibitor thapsigargin for 6 hours. Cell viability after thapsigargin (T9033; Sigma–Aldrich) exposure was first assessed using a 3-(4,5-dimethylthiazol-2-yl)-2,5-diphenyltetrazolium bromide assay, after which protein expression was analyzed by Western blot.

Antibodies

The full list of antibodies and the appropriate dilutions are provided in Supplemental Table 4.

Statistics

All values are expressed as mean±SD. Sample populations were tested for normality (Shapiro–Wilk test) and equality of variances (*F*-test). Two-group comparisons were performed using either the unpaired, two-tailed *t* test, with Welch correction in case of significantly different variance, or the Mann–Whitney test in case of non-normal distribution of the samples. Comparisons between three or more groups were performed using ordinary one-way ANOVA followed by Tukey-Kramer *post hoc* analysis, Brown–Forsythe ANOVA followed by Dunnett T3 *post hoc* analysis in case of significantly different variance, or Kruskal–Wallis followed by Dunn *post hoc* analysis in case of non-normal variance. P values ≤ 0.05 were considered statistically significant. Sample size was estimated on the basis of our published characterization of the C171Y and R186S mouse models,[11] in which group sizes ranging from $n=4$ to 24 were sufficient to detect biologically meaningful kidney and molecular phenotypes. Part of this study also represents an exploratory characterization of R186S mice crossed with *Lcn2*$^{+/-}$ mice. As such, sample sizes were determined by feasibility and animal availability inherent to the generation of a genetic cross. Animals were included on the basis of predefined genotype and age criteria required for each experimental group. No animals were excluded from the study after allocation unless they failed genotyping or did not meet predefined inclusion criteria. All animals meeting inclusion criteria were included in the analyses ($n=4$–16 per group) to maximize robustness while minimizing animal use, in accordance with Animal Research: Reporting of *In Vivo* Experiments guidelines and the principles of the 3Rs. No additional *a priori* exclusion criteria were applied at the animal level. As the characterization of the mouse models relies on knowledge of genotype, blinding was not implemented.

Study Approval

Animal procedures were carried out at the University of Zurich, Zurich, Switzerland, according to protocols approved by the Swiss Cantonal Veterinary Authority (approval number ZH049/17 and ZH195/20). For human studies, informed and written consent was obtained from all participants.

Results

Mutant UMOD Aggregates Induced LCN2 in Mouse Kidneys and Patient Urine

RNA-sequencing (RNA-seq) analyses of whole-kidney lysates identified *Lcn2* as the most significant upregulated gene in *Umod*$^{R186S/+}$ compared with *Umod*$^{+/+}$ kidneys at both 1 month and 4 months of age (Supplemental Figure 1A).[11] RT-qPCR confirmed a 25-fold increase in *Lcn2* mRNA at 1 month and 57-fold at 4 months (Figure 1A), alongside a 15-fold increase in LCN2 protein levels in the kidney at 4 months (Figure 1B), compared with *Umod*$^{+/+}$ littermates. By contrast, *Umod*$^{C171Y/+}$ mice —an ADTKD-*UMOD* model of mild severity—showed no significant changes in *Lcn2* mRNA or kidney LCN2 protein compared with controls (Figure 1, A and B). The *Umod*^{C125R} mice, which display an intermediate disease severity,[10] showed a three-fold increase in *Lcn2* mRNA at 1 month and 19-fold at 4 months (Figure 1A), and a three-fold increase in LCN2 protein levels in kidney at 4 months, compared with control littermates (Figure 1B). Urinary LCN2 levels were unchanged in *Umod*$^{C171Y/+}$ mice, markedly elevated in *Umod*$^{R186S/+}$ mice, and intermediate at 1 month in *Umod*$^{C125R/+}$ mice (Figure 1C). Immunofluorescence analysis revealed no detectable LCN2 signal in TAL cells in *Umod*$^{C171Y/+}$ and *Umod*$^{+/+}$ kidneys, a modest LCN2 signal in *Umod*$^{C125R/+}$ kidneys, and a strong LCN2 staining with UMOD accumulation in TAL cells of *Umod*$^{R186S/+}$ kidneys (Figure 1, D and E). In both *Umod*$^{+/+}$ kidneys and *Umod*$^{R186S/+}$, faint LCN2 staining was observed in proximal tubule cells and in Ly6G^{+}neutrophils (Figure 1E and Supplemental Figure 1, B and C).

Analysis across *Umod* genotypes revealed a strong positive association (r Pearson=0.88) between UMOD aggregate burden and kidney LCN2 protein levels, with *Umod*$^{+/+}$ and *Umod*$^{C171Y/+}$ kidneys showing no UMOD aggregation and progressively higher levels observed in *Umod*$^{C125R/+}$ and *Umod*$^{R186S/+}$ kidneys, respectively (Figure 1F).

To gain insight into mechanisms underlying LCN2 induction, we analyzed RNA-seq data from *Umod* kidneys for cellular stress and inflammation pathways (Supplemental Figure 2). *Umod*$^{R186S/+}$ kidneys displayed early activation of the unfolded protein response (UPR) at 1 month (Supplemental Figure 2A) and subsequent upregulation of NF-κB–dependent signaling at 4 months (Supplemental Figure 2B) compared with *Umod*$^{+/+}$ and *Umod*$^{C171Y/+}$, consistent with ER stress–driven LCN2 induction followed by inflammatory activation. The translational relevance of LCN2 induction was analyzed in a cohort of patients with ADTKD-*UMOD*. Urinary LCN2 levels were significantly higher in patients with ADTKD-*UMOD* compared with healthy controls (Figure 1G and Supplemental Figure 3; Supplemental Tables 1 and 2). The cohort included five distinct *UMOD* variants, three of which were represented by a single patient, limiting the ability to assess variant-specific differences or correlations with kidney function decline.

Together, these results indicate that LCN2 is strongly induced in kidney and urine, related to specific *UMOD* variants that drive the accumulation of toxic UMOD aggregates in TAL cells.

Clearance of Mutant UMOD Lowered LCN2 Levels in Tubular Cells

We next investigated the mechanism of LCN2 induction in kidney tubular cells using the established system of immortalized mIMCD-3 cells transduced with GFP-tagged human WT or mutant (p.R185S, p.C170Y) *UMOD*.[11] Immunofluorescence of *UMOD*-expressing cells showed co-localization of R185S mutant UMOD aggregates with the ER marker calreticulin, whereas WT UMOD localized mainly at the plasma membrane, while C170Y cells showed an intermediate phenotype (Figure 2A). Both R185S and C170Y cells exhibited increased intracellular LCN2-positive structures compared with WT cells, with a

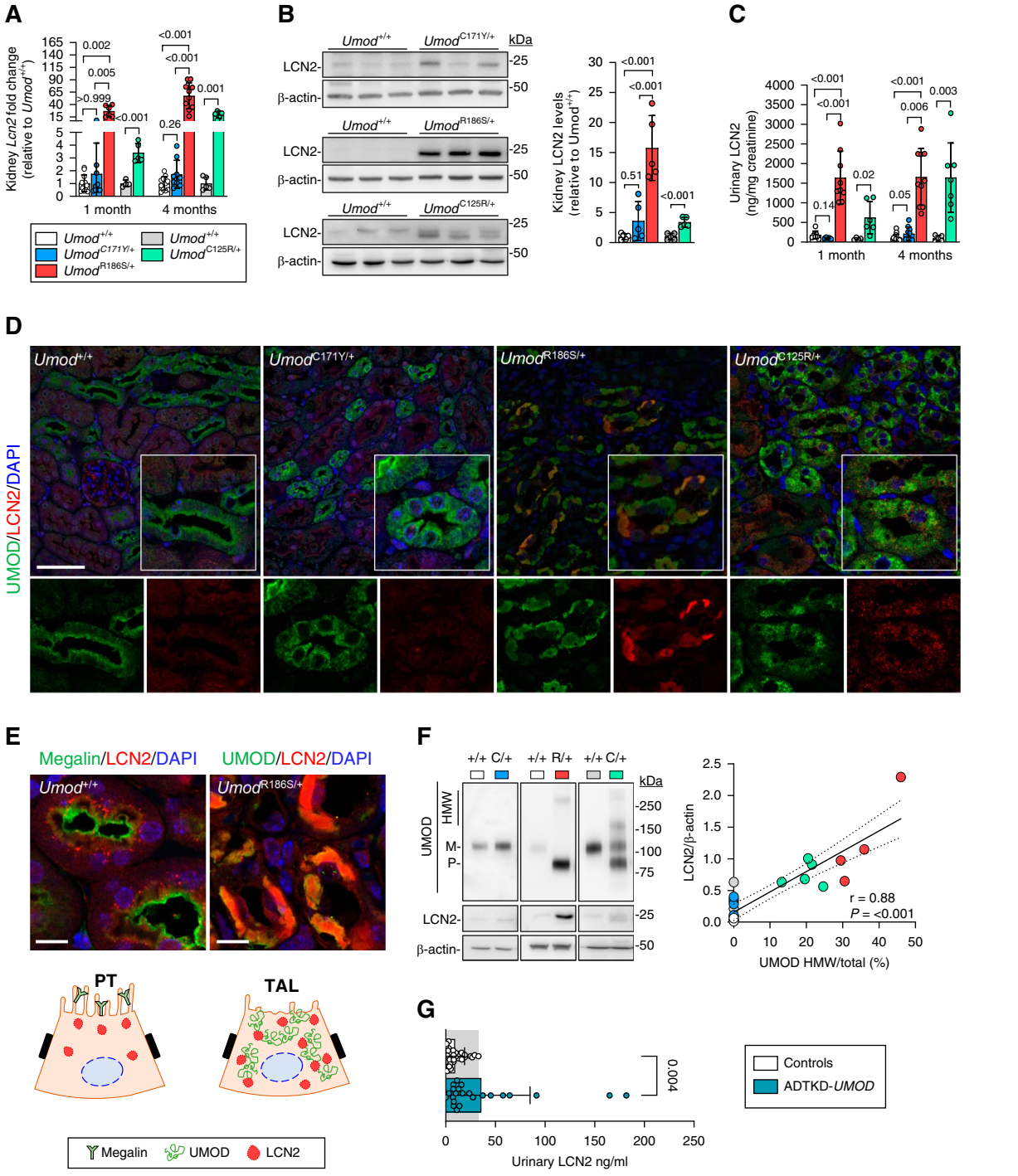

Figure 1. UMOD variants are associated with LCN2 induction in *Umod* KI mice and patients with ADTKD-*UMOD*. (A) *Lcn2* transcript levels evaluated by RT-qPCR on total kidney extracts from 1- to 4-month-old *Umod* KI mice (n=4–12 animals per group). Bars indicate mean±SD. For $Umod^{+/+}$, $Umod^{C171Y}$, $Umod^{R186S}$: Kruskal–Wallis with Dunn *post hoc* analysis (1 month) and Brown–Forsythe ANOVA with Dunnett T3 *post hoc* test (4 months). For $Umod^{+/+}$, $Umod^{C125R}$: unpaired, two-tailed *t* test (1 month) or unpaired *t* test with Welch correction (4 months). (B) Immunoblot analysis of kidney LCN2 in 4 months *Umod* KI mice. β-actin was used as a loading control (n=5 animals per group). Densitometry analysis relative to respective $Umod^{+/+}$. Bars indicate mean±SD. For $Umod^{+/+}$, $Umod^{C171Y}$, $Umod^{R186S}$: ordinary one-way ANOVA with Tukey *post hoc* test. For $Umod^{+/+}$, $Umod^{C125R}$: unpaired, two-tailed *t* test. (C) LCN2 urinary levels evaluated by ELISA and normalized on creatinine from 1- to 4-month-old *Umod KI* mice (n=4–15 animals per group). Bars indicate mean±SD. For $Umod^{+/+}$, $Umod^{C171Y}$, $Umod^{R186S}$: Brown–Forsythe ANOVA with Dunnett T3 *post hoc* test (1 month) and Kruskal–Wallis with Dunn *post hoc* analysis (4 months). For $Umod^{+/+}$, $Umod^{C125R}$: unpaired *t* test with Welch correction. (D) Representative immunofluorescence of LCN2 (red) and UMOD (green) on kidney sections from 4-month-old *Umod* KI mice. Nuclei are counterstained with DAPI (blue). Scale bar: 50 μm (n=3 animals per group). (E) Representative high magnification immunofluorescence of LCN2 and diagram illustrating LCN2 (red) localization in the PT and the TAL of the loop of Henle. In endogenous

Figure 1. *Continued.* conditions, a few proximal tubules display LCN2 apical staining colocalization with megalin (green), while in *Umod*$^{R186S/+}$ mice, multiple TAL show intracellular overexpression of LCN2 colocalizing with UMOD (green). Scale bar: 10 μm. (F) Left: representative immunoblots for UMOD and LCN2 in kidneys from 4-month *Umod* KI *mice*. β-actin was used as a loading control (n=4–5 animals per group). Right: linear regression (black line) representing the correlation between UMOD aggregates and LCN2 kidney levels in *Umod* KI mice. The dotted lines show the 95% CIs. Dots represent individual animals. The equation for the curve is $Y=0.03211*X+0.1565$; R^2=0.78; Pearson r=0.88; P (two-tailed) < 0.001. (G) LCN2 urinary levels evaluated by ELISA in a subset of healthy controls (n=31) and patients with ADTKD-*UMOD* (n=23). Gray area indicates normal (healthy) range. Bars indicate mean±SD. Mann–Whitney test. ADTKD-*UMOD*, autosomal dominant tubulointerstitial kidney disease due to pathogenic *UMOD*; CI, confidence interval; DAPI, 4′,6-diamidino-2-phenylindole; HMW, high molecular weight; KI, knock-in; LCN2, lipocalin-2; M, mature; P, precursor; PT, proximal tubule; TAL, thick ascending limb; UMOD, uromodulin.

more pronounced induction observed in R185S cells (Figure 2A). Analysis of expression of *Lcn2* at both the mRNA and protein levels confirmed a substantial overexpression in R185S cells relative to both WT and C170Y cells (Figure 2, B and C). To confirm that LCN2 induction in tubular cells can result from ER stress triggered by protein aggregation, we treated *UMOD* WT cells with thapsigargin, a general ER stress inducer (Supplemental Figure 4). This treatment increased LCN2 expression and upregulated the ER stress marker GRP78 while, in parallel, decreasing the mature form and increasing the premature form of UMOD—consistent with ER stress affecting protein processing (Supplemental Figure 4B). We previously demonstrated that stimulating autophagy, *e.g.*, through mTORC1 inhibition, improved the clearance of mutant UMOD.[11] Accordingly, we tested if autophagy activation could impact LCN2 induction in *UMOD*-expressing cells. Treatment with the mTORC1 inhibitor Torin1 significantly reduced both UMOD aggregates and core, paralleled by a decrease of LCN2 and mTORC1 activation (p4EBP1) in R185S and C170Y cells (Figure 2, D and E, and Supplemental Figure 5). These results suggest that LCN2 induction is linked to aggregate-associated cellular stress and support a model in which the propensity of specific UMOD mutants to form aggregates drives ER stress, in turn inducing LCN2 in mouse and cellular models of ADTKD-*UMOD*.

Effects of *Lcn2* Deletion on Kidney Function Parameters in *Umod*$^{R186S/+}$ Mice

Considering the magnitude of induction of LCN2 and its potential involvement in CKD progression, we hypothesized that LCN2 could participate to kidney damage in ADTKD-*UMOD* (Figure 3A). To investigate this hypothesis, we crossed *Umod*$^{R186S/+}$ mice with *Lcn2*$^{+/-}$ mice to obtain *Umod*$^{R186S/+}$*Lcn2*$^{-/-}$ mice and appropriate littermate controls (Figure 3B). The LCN2 deletion was confirmed by immunoblot and immunofluorescence analyses (Figure 3, C and D). As previously described, *Umod*$^{R186S/+}$ mice develop early kidney dysfunction, characterized by increased BUN levels and impaired urinary concentrating ability (polyuria/polydipsia, decreased urinary osmolality) by 4 months of age (Figure 3E and Table 1).[11] Analysis of clinical and biochemical parameters indicated that the deletion of LCN2 had no significant effect in the *Umod*$^{+/+}$*Lcn2*$^{-/-}$ compared with *Umod*$^{+/+}$*Lcn2*$^{+/+}$ mice (Figure 3E and Table 1). Similarly, deletion of *Lcn2* had no significant effect on the phenotype observed in *Umod*$^{R186S/+}$ mice (Figure 3E and Table 1). Taken together, these results suggest that the genetic deletion of *Lcn2* is not improving kidney function parameters in *Umod*^{R186S} mice.

Effects of *Lcn2* Deletion on Development of Kidney Lesions in *Umod*^{R186S} Mice

We next examined whether the deletion of LCN2 in *Umod*$^{R186S/+}$ mice influences hallmarks of kidney injury in the context of ADTKD-*UMOD*. At 1 month, no significant fibrosis was observed in either *Umod*$^{R186S/+}$*Lcn2*$^{+/+}$ and *Umod*$^{R186S/+}$*Lcn2*$^{-/-}$ kidneys (Figure 4A and Supplemental Figure 6A). By 4 months, analysis of Picrosirius red staining revealed comparable levels of interstitial fibrosis in both genotypes, reaching 15%–17% of fibrosis area (Figure 4A). Signs of inflammation were present at 1 month, with an increased number of CD3$^+$ lymphocytes in proximity to UMOD-positive TAL segments in both *Umod*$^{R186S/+}$*Lcn2*$^{+/+}$ and *Umod*$^{R186S/+}$*Lcn2*$^{-/-}$ kidneys compared with *Umod*$^{+/+}$*Lcn2*$^{+/+}$ controls (Figure 4A and Supplemental Figure 6A). At 4 months, a similar progression of interstitial infiltrates was observed in both mutant mice (Figure 4A). Analysis of the inflammatory signatures of the *Umod*$^{R186S/+}$ kidneys revealed a mild induction of the Nfκ-b subunit *Relb* (1.8-fold) at 1 month, only in *Umod*$^{R186S/+}$*Lcn2*$^{+/+}$ kidneys compared with WT kidneys (Supplemental Figure 6B). Multiple inflammation markers were upregulated at 4 months, with no significant differences because of the loss of LCN2 (Figure 4B). Furthermore, the deletion of LCN2 did not affect on the upregulation of the UPR gatekeeper protein GRP78 and the protein kinase RNA-like ER kinase branch of the UPR in *Umod*$^{R186S/+}$*Lcn2*$^{-/-}$ kidneys at 4 months (Figure 4C). In addition, the pattern of mutant UMOD accumulation was similar in the *Umod*$^{R186S/+}$*Lcn2*$^{-/-}$ compared with *Umod*$^{R186S/+}$*Lcn2*$^{+/+}$ kidneys (Figure 4D). Collectively, these data indicate that the deletion of LCN2 does not influence UMOD accumulation nor multiple markers of kidney damage progression in the *Umod*^{R186S} mouse model.

LCN2 Participates in Iron Dysregulation but Not Ferroptosis in *Umod*$^{R186S/+}$ Kidneys

Since LCN2 regulates iron homeostasis and excess free iron can contribute to kidney injury, we investigated whether *Umod*^{R186S} kidneys show iron dysregulation and whether this is influenced by LCN2 (Figure 5A). Kidney sections were stained by Perls Prussian blue reaction, which detects mostly ferric iron, the low solubility form of iron (Figure 5B and Supplemental Figure 7). In control kidneys

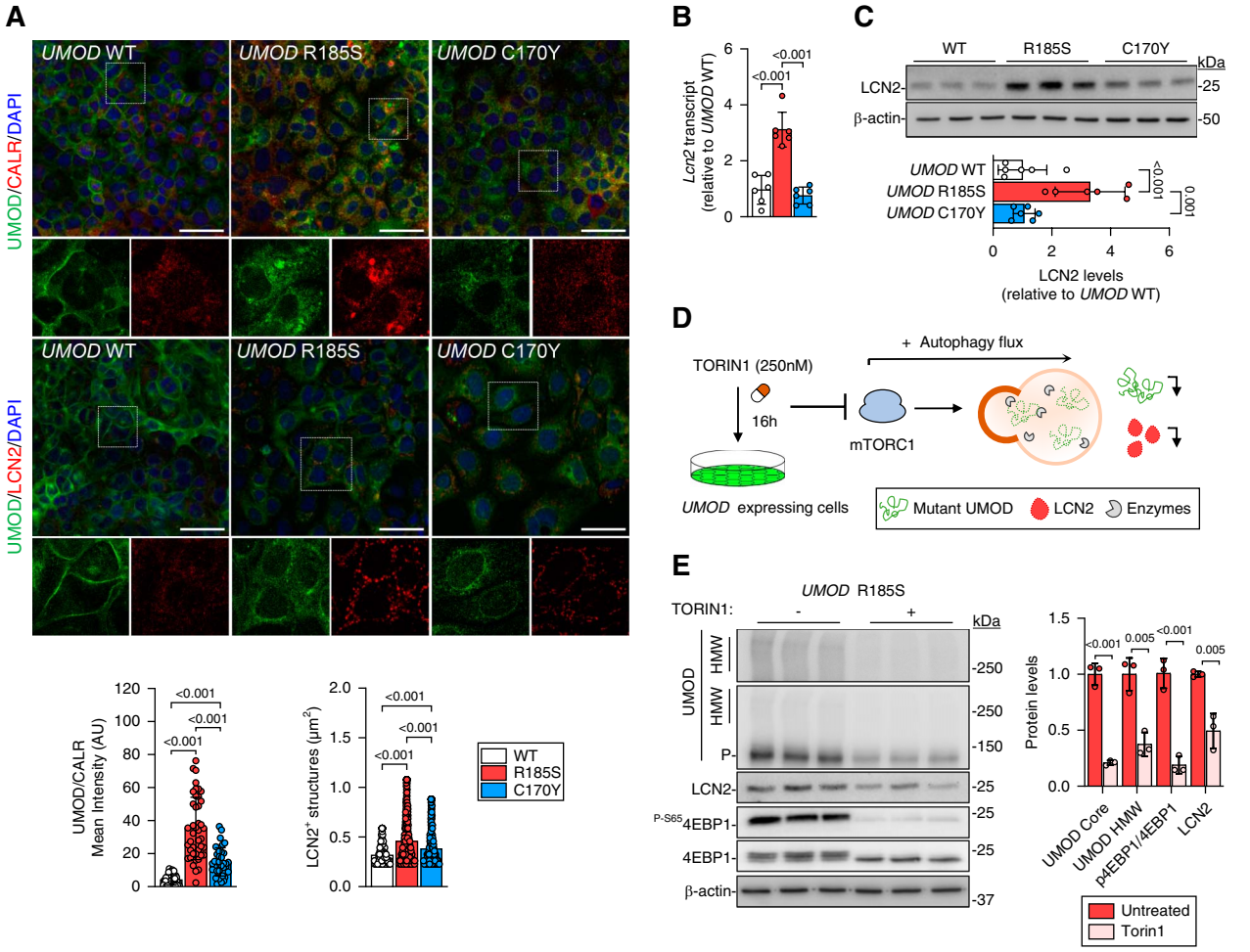

Figure 2. Specific UMOD variants drive aggregate formation and LCN2 expression in mIMCD cells. (A) Immunofluorescence analysis of UMOD (green) and Calreticulin or LCN2 (red) in UMOD-expressing cells. Nuclei are counterstained with DAPI (blue). Scale bar: 30 um (n=30–60 cells per condition). Separate channels are shown below each panel. Bars indicate mean±SD. Kruskal–Wallis with Dunn *post hoc* analysis, compared with *UMOD* WT cells. (B) *Lcn2* transcript levels evaluated by RT-qPCR in UMOD-expressing cells (n=6 per cell line). Values are relative to *UMOD* WT cells. Bars indicate mean±SD. Ordinary one-way ANOVA with the Tukey *post hoc* test. (C) Immunoblotting for LCN2 in UMOD-expressing cells. β-actin was used as a loading control. Densitometry analysis relative to *UMOD* WT cells. Bars indicate mean±SD. One-way ANOVA with the Tukey *post hoc* test. (D) Diagram illustrating autophagy induction through Torin1 treatment. Aggregated mutant UMOD is delivered to the autolysosome for degradation, resulting in reduced LCN2 induction on autophagy activation. (E) Immunoblotting for UMOD, mTORC1 target p4EBP1 protein, and LCN2 in *UMOD* R185S-expressing cells. β-actin was used as a loading control. Bars indicate mean±SD. Unpaired, two-tailed t test or unpaired t test with Welch correction. CALR, Calreticulin; WT, wild-type.

($Umod^{+/+}Lcn2^{+/+}$ and $Umod^{+/+}Lcn2^{-/-}$), no detectable iron deposits were observed, consistent with normal iron handling. By contrast, multiple iron deposits were detected in $Umod^{R186S/+}Lcn2^{+/+}$ kidneys, suggesting dysregulated iron homeostasis in the ADTKD-*UMOD* model. Interestingly, iron accumulation was markedly reduced in $Umod^{R186S/+}Lcn2^{-/-}$ kidneys, as shown by decreased Fe^{3+} signal intensity (Figure 5B). Most of the iron-positive structures were located in the vicinity of TAL profiles accumulating mutant UMOD (Figure 5B). These results suggest that iron clusters involving LCN2 are found near damaged TAL segments and that LCN2 contributes to the iron accumulation observed in $Umod^{R186S}$ kidneys.

Investigation of iron metabolism gene expression revealed a downregulation of *Dmt1*, the major iron importer, in 1-month-old $Umod^{R186S/+}Lcn2^{+/+}$ and $Umod^{R186S/+}Lcn2^{-/-}$ kidneys compared with $Umod^{+/+}Lcn2^{+/+}$ controls (Supplemental Figure 7B), suggesting that iron uptake through this pathway is reduced in the mutant kidneys—but not affected by *Lcn2* deletion. At 4 months, $Umod^{R186S/+}$ kidneys showed increased expression of *Hfe*, a regulator of hepcidin signaling, along with continued downregulation of *Dmt1* independently of *Lcn2* status (Figure 5C). However, in $Umod^{R186S/+}Lcn2^{-/-}$ kidneys, we observed a distinct iron-handling signature: a significant upregulation of *Slc40a1*, encoding the iron exporter ferroportin, and downregulation of *Tfrc*, the transferrin receptor, compared with $Umod^{+/+}Lcn2^{+/+}$ kidneys (Figure 5C). This expression pattern supports a shift toward reduced iron uptake and enhanced iron export in the absence of LCN2, which may underlie the decreased iron accumulation observed in these mice (Figure 5B).

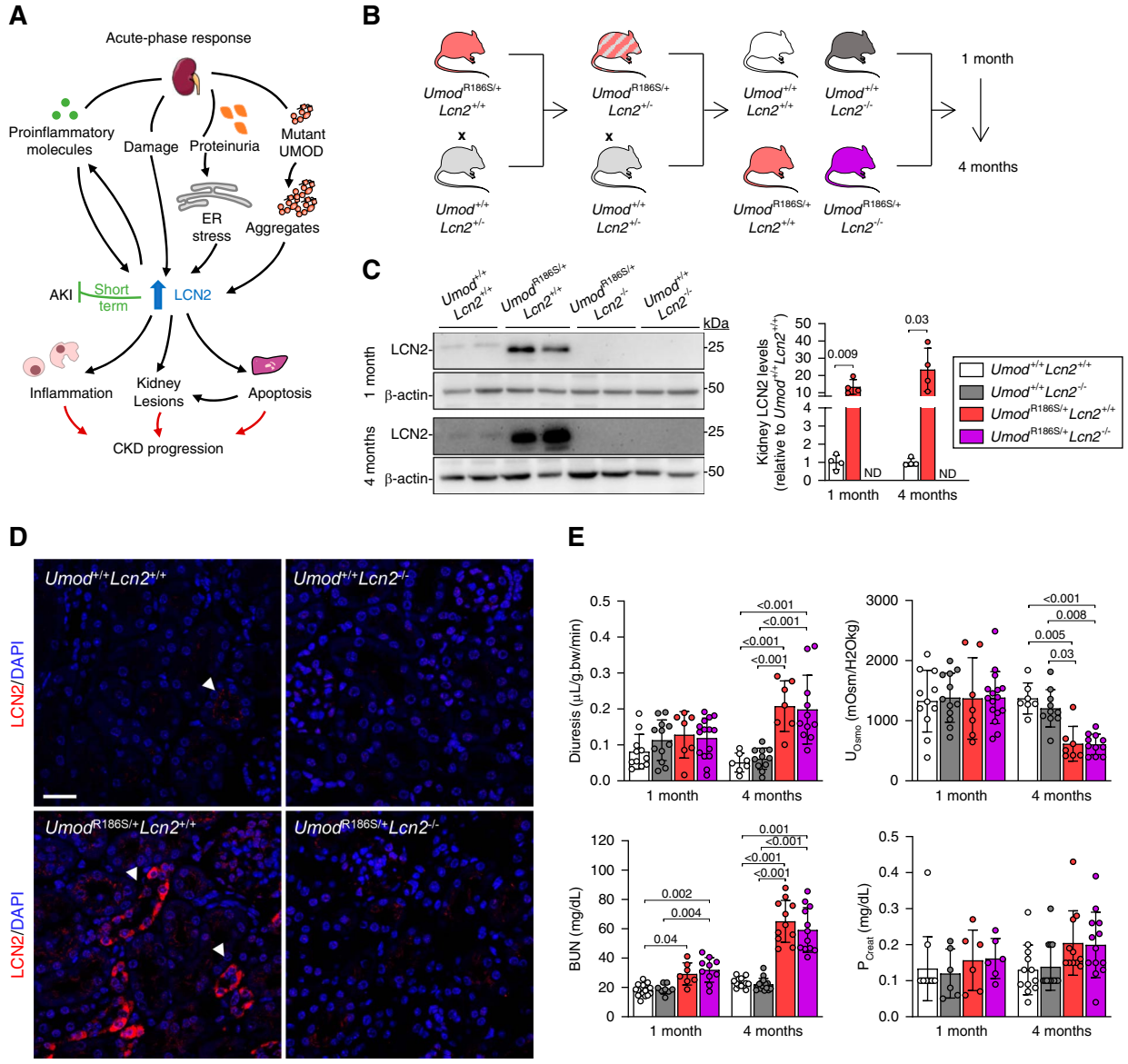

Figure 3. Effect of LCN2 deletion on kidney function parameters in the *Umod*$^{R186S/+}$ mice. (A) Diagram showing the pathogenic roles of LCN2 in the kidney. LCN2 levels increase during the acute phase response triggered by harmful stimuli, causing apoptosis, kidney lesions, and inflammation—all contributing to CKD progression. Short-term beneficial effects in limiting AKI have also been reported. (B) Crossing strategy for generation of *Umod*$^{R186S/+}$; *Lcn2*$^{-/-}$ mice. (C) Immunoblot analysis of kidney LCN2 in 1 and 4 months *Umod*$^{R186S/+}$ mice. β-actin was used as a loading control (n=4 animals per group). Densitometry analysis relative to *Umod*$^{+/+}$; *Lcn2*$^{+/+}$. Bars indicate mean±SD. Unpaired t test with Welch correction (1 month) or Mann–Whitney test (4 months). (D) Representative immunofluorescence of LCN2 (red) on kidney sections from 1-month-old mice. Nuclei are counterstained with DAPI (blue). Scale bar: 25 µm (n=3 animals per group). (E) Diuresis, urinary osmolality BUN, and plasma creatinine (P_{Creat}) in *Umod*$^{R186S/+}$ mice at 1 and 4 months (n=7–16 animals per group). Bars indicate mean±SD. Ordinary one-way ANOVA with the Tukey *post hoc* test or Brown–Forsythe ANOVA with the Dunnett T3 *post hoc* test, or Kruskal–Wallis with Dunn *post hoc* analysis. ER, endoplasmic reticulum.

Because iron load can lead to ferroptosis, an iron-dependent cell death, we investigated whether the deletion of LCN2 had any effect on ferroptosis inducers and repressors in the *Umod*$^{R186S/+}$ kidneys (Figure 5D). In fact, similar inductions of the ferroptosis-related *Slc7a11* (112-130-fold), the transcription factor *Atf4*, implicated in ER stress and antiferroptotic pathways and *Nupr1*, a stress-inducible transcription factor driving ferroptotic resistance, were observed in both *Umod*$^{R186S/+}$; *Lcn2*$^{+/+}$ and *Umod*$^{R186S/+}$; *Lcn2*$^{-/-}$ kidneys.[27–29] As iron-mediated reactive oxygen species production can lead to ferroptosis,[30] we investigated the protein expression of the oxidative stress markers heme oxygenase-1 and SOD1, which were unchanged in *Umod*$^{R186S/+}$ kidneys (Figure 5E).

These results suggest that LCN2 participates in iron dysregulation in *Umod*^{R186S} mice. However, the deletion of LCN2 is not reflected by significant changes in ferroptosis.

Table 1. Effects of lipocalin-2 deletion on clinical and biological parameters in *Umod* mice

Parameter	1-Month-Old				4-Month-Old			
	Umod$^{+/+}$ *Lcn2*$^{+/+}$	*Umod*$^{+/+}$ *Lcn2*$^{-/-}$	*Umod*$^{R186S/+}$ *Lcn2*$^{+/+}$	*Umod*$^{R186S/+}$ *Lcn2*$^{-/-}$	*Umod*$^{+/+}$ *Lcn2*$^{+/+}$	*Umod*$^{+/+}$ *Lcn2*$^{-/-}$	*Umod*$^{R186S/+}$ *Lcn2*$^{+/+}$	*Umod*$^{R186S/+}$ *Lcn2*$^{-/-}$
	n=11 (4F/7M)	*n*=12 (5F/7M)	*n*=7 (6F/1M)	*n*=16 (5F/11M)	*n*=7 (1F/6M)	*n*=11 (5F/6M)	*n*=7 (3F/4M)	*n*=11 (4F/7M)
Body weight, g	17.9±0.6	17.1±0.6	16.5±0.5	17.6±0.5	30±2	30±2	27±2	27±1
Water intake, µl/min per g.bw	0.39±0.03	0.36±0.02	0.36±0.03	0.34±0.01	0.17±0.01	0.18±0.01	0.37±0.03 $P < 0.001$	0.34±0.03 $P = 0.001$
Urine								
Diuresis, µL/g.bw per min	0.08±0.01	0.11±0.02	0.13±0.02	0.11±0.01	0.05±0.008	0.06±0.009	0.21±0.02 $P < 0.001$	0.20±0.03 $P = 0.001$
Na^+, g/g.creat	8.8±0.5	7.0±0.4 $P = 0.02$	9±1	8.2±0.4	4.9±0.5	4.5±0.3	4.8±0.8	5.0±0.4
K^+, g/g.creat	30.2±0.8	29±1	32±2	28±1	19±2	18±1	19±2	20.7±0.9
Cl^-, g/g.creat	25.7±0.7	25±3	28±2	23.9±0.9	14±2	12.3±0.9	14±1	15±1
Ca^{2+}, g/g.creat	0.23±0.02	0.20±0.02	0.41±0.04 $P = 0.001$	0.30±0.02[a] $P = 0.02$	0.13±0.02	0.14±0.02	0.24±0.02 $P = 0.003$	0.25±0.02 $P = 0.004$
Creatinine, mg/dL	23±2	27±2	25±6	27±2.0	38±3	38±4	18±5 $P = 0.010$	16±2 $P < 0.001$
Osmolality, mOsm per kg H_2O	1325±147	1383±113	1371±237	1375±104	1371±62	1207±93	617±111 $P < 0.001$	607±49 $P < 0.001$
	n=6 (1F/5M)	*n*=7 (5F/2M)	*n*=7 (6F/1M)	*n*=7 (3F/4M)	*n*=7 (1F/6M)	*n*=7 (5F/2M)	*n*=7 (3F/4M)	*n*=7 (2F/5M)
LCN2, ng/mg. Creat	313±22	BDR	1374±220 $P = 0.002$	BDR	115±11	BDR	1303±144 $P < 0.001$	BDR
Plasma	*n*=16 (5F/11M)	*n*=8 (4F/4M)	*n*=7 (6F/1M)	*n*=10 (4F/6M)	*n*=13 (4F/9M)	*n*=15 (6F/9M)	*N*=11 (6F/5M)*B*	*n*=13 (6F/7M)
Na^+, mmol/L	146±0.8	145±0.6	143±1	145±0.6[b]	147±0.7[b]	147±0.6[b]	149±0.9	149±0.5 $P = 0.03$
K^+, mmol/L	9.5±0.6	8.1±0.7	12±1	9.6±0.3	8±1	8.4±0.7	7.5±0.4	7.9±0.4
Cl^-, mmol/L	107±0.8	109±0.5	105±1	107±0.7	110±0.6	110±0.5	106±0.8 $P = 0.005$	107±0.7
Ca^{2+}, mg/dL	11.0±0.2	10.8±0.2	10.6±0.4	10.9±0.2	9.9±0.2	9.8±0.2	10.7±0.2 $P = 0.009$	10.5±0.2
Creatinine, mg/dL	0.13±0.02[c]	0.12±0.03[d]	0.16±0.02[d]	0.14±0.03[e]	0.14±0.02[b]	0.13±0.02[d]	0.21±0.03 $P = 0.04$	0.20±0.02 $P = 0.04$
BUN, mg/dL	18±1	19±1	29±3 $P < 0.001$	32±3 $P < 0.001$	23±1	22±1	66±4 $P < 0.001$	59±4 $P < 0.001$

Data±SEM. BDR, below detection range; LCN2, lipocalin-2; *t* test, *P* versus *Umod*$^{+/+}$.
[a]*P Lcn2*$^{+/+}$*Umod*$^{R186S/+}$ versus *Lcn2*$^{-/-}$*Umod*$^{R186S/+}$.
[b]One sample was undetectable.
[c]Four samples were undetectable.
[d]Two samples were undetectable.
[e]Three samples were undetectable.

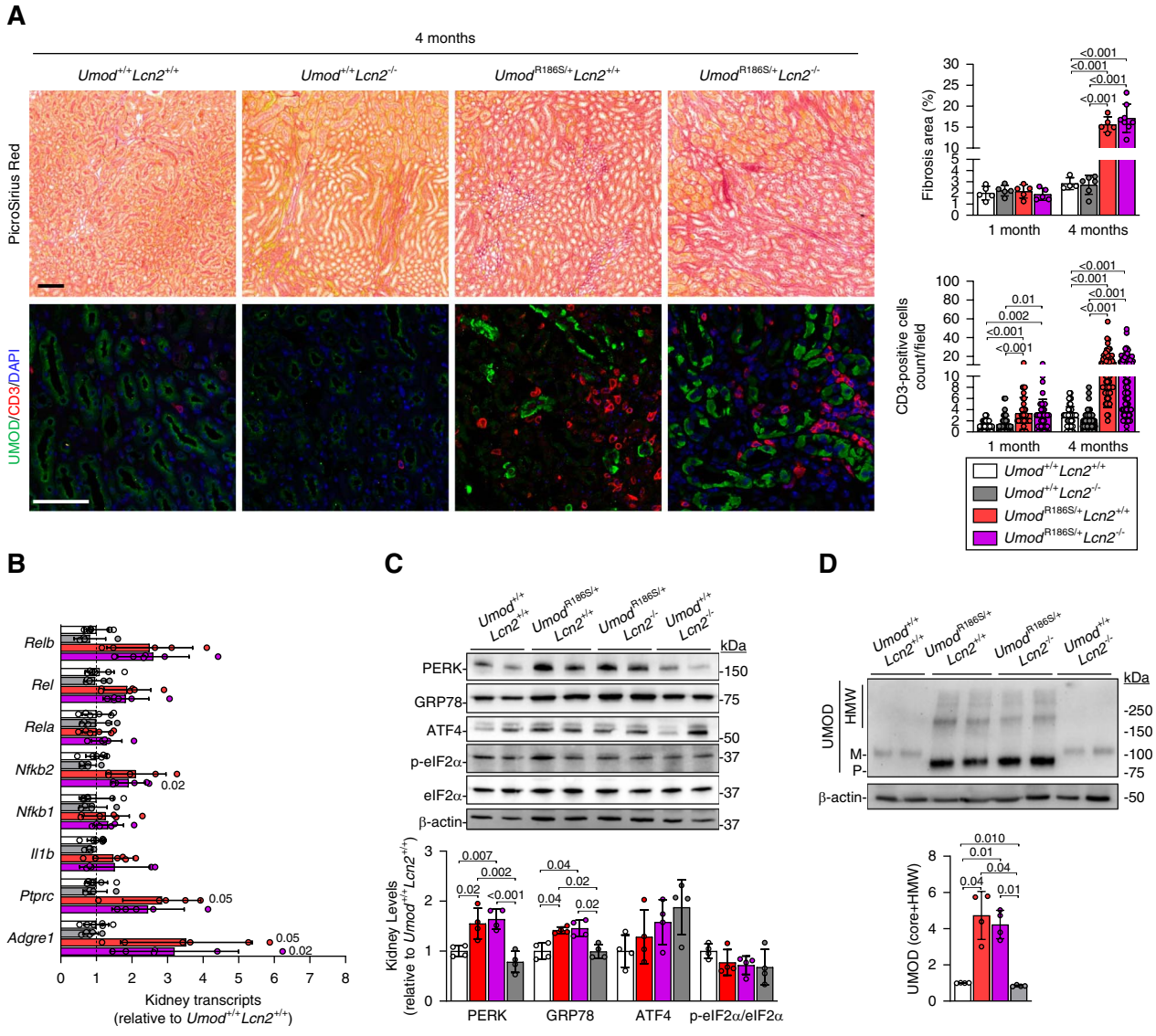

Figure 4. Effect of LCN2 deletion on UMOD processing and kidney damage pathways in the *Umod*$^{R186S/+}$ mice. (A) Fibrosis and inflammation in 4-month-old *Umod*$^{R186S/+}$ mice. Upper panel: Picrosirius red staining of kidney sections showing accumulation of interstitial collagen fibers (red) and quantification of the collagen-positive area over the total tissue at 1 month and 4 months. Scale bar: 100 μm (n=4–8 animals per group). Bars indicate mean±SD. Ordinary one-way ANOVA with the Tukey *post hoc* test. Lower: immunofluorescence of UMOD (green) and CD3 (red) on kidney sections and quantification of the CD3$^+$ infiltrates per field at 1 and 4 months. Nuclei are counterstained with DAPI (blue). Scale bar: 50 μm (n=3–4 animals per group). Bars indicate mean±SD. Kruskal–Wallis with Dunn *post hoc* analysis. (B) Transcript levels of inflammation markers evaluated by RT-qPCR on total kidney extracts from mice at 4 months (n=5–6 animals per group). Bars indicate mean±SD. Ordinary one-way ANOVA with the Tukey *post hoc* test or Brown–Forsythe ANOVA with the Dunnett T3 *post hoc* test, or Kruskal–Wallis with Dunn *post hoc* analysis. (C) Representative immunoblot analysis of ER stress markers in 4-month-old kidney lysates of *Umod*$^{R186S/+}$ mice (n=4 animals per group). β-actin used as loading control. Densitometry analysis is relative to *Umod*$^{+/+}$; *Lcn2*$^{+/+}$. Bars indicate mean±SD. Ordinary one-way ANOVA with the Tukey *post hoc* test or Brown–Forsythe ANOVA with the Dunnett T3 *post hoc* test, or Kruskal–Wallis with Dunn *post hoc* analysis. (D) Immunoblot analysis of kidney UMOD in 4-month-old mice. β-actin was used as a loading control (n=4 animals per group). Densitometry analysis is relative *to Umod*$^{+/+}$; *Lcn2*$^{+/+}$. The mature and precursor UMOD are collectively referred to as the core. Bars indicate mean±SD. Brown–Forsythe ANOVA with Dunnett T3 *post hoc* test. *Adgre1*, adhesion G protein–coupled receptor E1; *Il1b*, IL 1 β; *Nfkb1*, NF kappa B subunit 1; *Nfkb2*, NF kappa B subunit 2; PERK, protein kinase RNA-like ER kinase; *Ptprc*, protein tyrosine phosphatase receptor type C.

LCN2 Did Not Affect Mitochondrial Dynamics in *Umod*$^{R186S/+}$ Kidneys

Given that LCN2 was shown to promote mitochondrial dysfunction in models of AKI,[31] we investigated mitochondrial dynamics in the presence and absence of *Lcn2* in the *Umod*^{R186S} model. Immunoblot analysis of kidney lysates at 4 months revealed no significant changes in either profusion markers (MFN2, OPA1) or in total

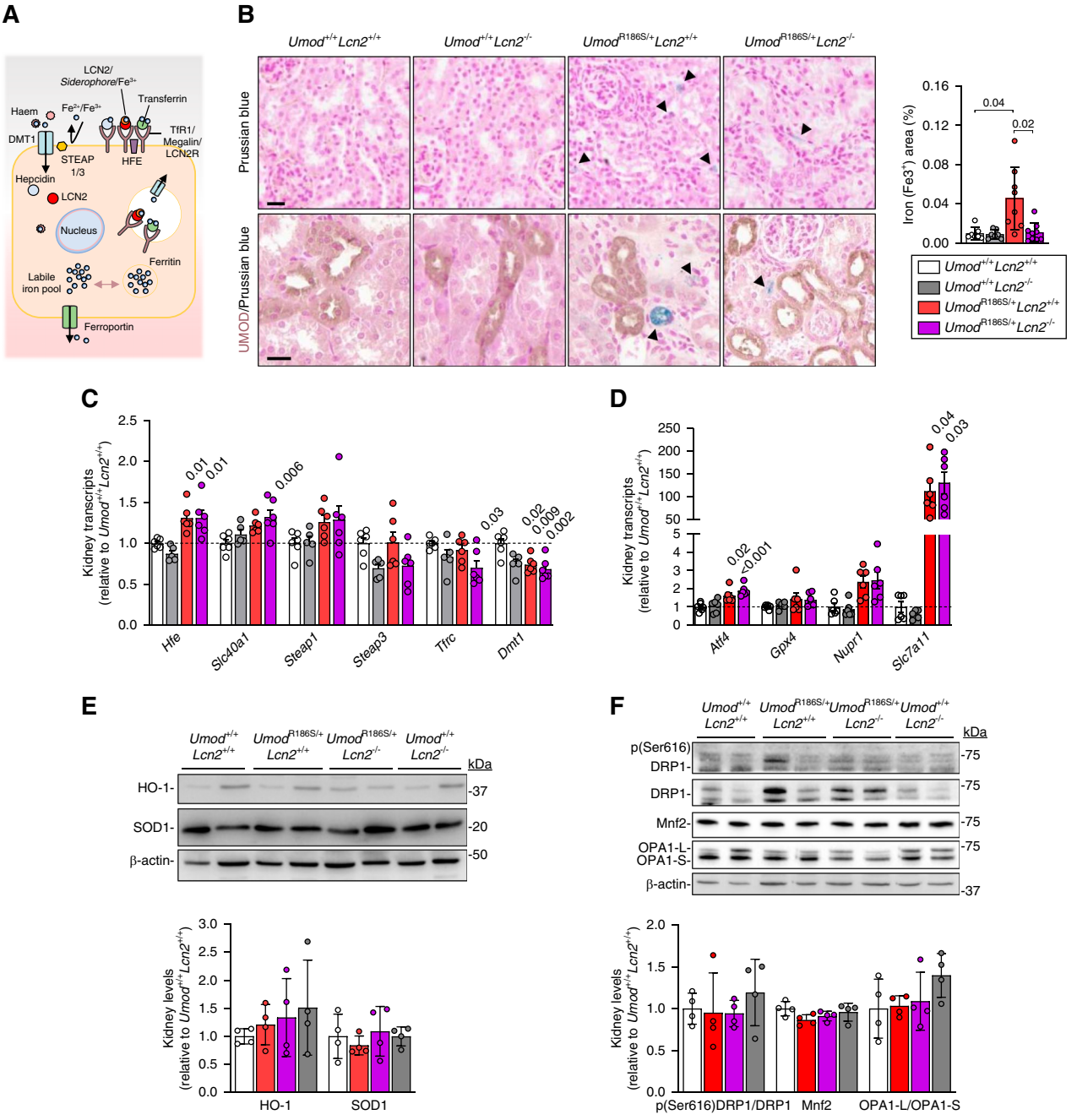

Figure 5. Effect of LCN2 deletion on iron homeostasis and mitochondrial dynamics in the *Umod*$^{R186S/+}$ mice. (A) Diagram illustrating iron transport in the cell. Iron enters the cell through iron importers such as DMT1 or by receptor-mediated endocytosis and can join the labile iron pool or be stored through ferritin. Iron is exported into the circulation through exporters such as ferroportin. (B) Left: Prussian blue staining (upper panel) and immunohistochemical staining of UMOD (brown) combined with Prussian blue (blue; lower panel) in 4-month-old *Umod*$^{R186S/+}$ kidneys. Nuclei are counterstained with nuclear fast red. Scale bar: 20 μm (n=7–9 animals per group). Black arrows show region of interest. Right: quantification of the iron-positive area over the total tissue. Kruskal–Wallis with Dunn *post hoc* analysis. Bars indicate mean±SD. (C) Transcript levels of iron metabolism markers evaluated by RT-qPCR on total kidney extracts from 4-month-old mice (n=5–6 animals per group). Bars indicate mean±SD. Ordinary one-way ANOVA with the Tukey *post hoc* test. *P* on the graph: comparison with *Umod*$^{+/+}$; *Lcn2*$^{+/+}$. (D) Transcript levels of ferroptosis-related molecules evaluated by RT-qPCR on total kidney extracts from 4-month-old mice (n=6 animals per group). Bars indicate mean±SD. *Gpx4, Nupr1, Slc7a11*: Kruskal–Wallis with Dunn *post hoc* analysis. *P* on the graph: comparison with *Umod*$^{+/+}$; *Lcn2*$^{+/+}$. (E) Immunoblot analysis of HO-1 and SOD1 levels in 4-month-old mice. β-actin was used as a loading control (n=4 animals per group). Densitometry analysis is relative *to Umod*$^{+/+}$; *Lcn2*$^{+/+}$. Bars indicate mean±SD. Ordinary one-way ANOVA with the Tukey *post hoc* test. (F) Immunoblot analysis of mitochondrial profission and profusion markers in 4-month-old mice (n=4 animals per group). Densitometry analysis is relative *to Umod*$^{+/+}$; *Lcn2*$^{+/+}$. Bars indicate mean±SD. Ordinary one-way ANOVA with the Tukey *post hoc* test or Brown–Forsythe ANOVA with the Dunnett T3 *post*

Figure 5. *Continued.* *hoc* test. *Atf4*, one-way ANOVA with the Tukey *post hoc* test; *Dmt1*, divalent metal transporter 1; *Hfe*, homeostatic iron regulator; HO-1, heme oxygenase-1; *Slc40a1*, solute carrier family 40 member 1; *Steap1*, six-transmembrane epithelial antigen of prostate 1; *Steap3*, six-transmembrane epithelial antigen of prostate 3; *Tfrc*, transferrin receptor.

DRP1 levels and the phospho-DRP1/DRP1 ratio in *Umod*$^{R186S/+}$ kidneys, regardless of LCN2 presence, and no differences compared with their respective controls at 4 months of age (Figure 5F).

Discussion

The availability of representative KI mouse models provides the opportunity to investigate potential mechanisms involved in the progression of ADTKD-*UMOD*. Unbiased expression studies in *Umod*^{R186S} mice, a model of rapidly progressing ADTKD-*UMOD*, evidenced a major upregulation of LCN2 in the kidney and urine. This induction occurs in TAL cells, correlating with the level of mutant UMOD aggregation. Urinary LCN2 is also elevated in patients with ADTKD-*UMOD*, with specific *UMOD* variants apparently associated with higher LCN2 levels. Studies in immortalized mIMCD cells stably transfected with *UMOD* variants substantiated the link between mutant UMOD accumulation, aggregate formation, ER stress, and induction of LCN2. By genetically deleting LCN2 in the *Umod*$^{R186S/+}$ mice, we verified a significant impact of LCN2 on iron deposits and homeostasis in mutant kidneys, but no effect on defective UMOD processing, damaging pathways, structural damage, and kidney failure progression in these mice. Thus, LCN2 reflects tubular stress and effects on iron handling but does not influence disease progression in mouse models of ADTKD-*UMOD*.

Our set of ADTKD-*UMOD* mouse models and kidney tubular cell systems revealed that LCN2 induction closely parallels the propensity of mutant UMOD to form intracellular aggregates. These observations align with allele-specific aggregation toxicity and disease progression in ADTKD-*UMOD*.[11] Mechanistic studies in *UMOD*-expressing tubular cells suggested that LCN2 induction occurs in response to intracellular mutant UMOD aggregates, with a more pronounced effect in R185S-expressing cells than C170Y. Notably, activation of autophagy through mTORC1 inhibition with Torin1 reduced both UMOD aggregates and LCN2 expression, supporting a model where the UMOD aggregate burden directly drives LCN2 induction. These results highlight LCN2 as a sensitive marker of intracellular proteotoxic stress, reflecting the severity of mutant UMOD accumulation across mouse models, cell systems, and human disease.

Because LCN2 behaves as an acute phase protein triggered by a variety of stress situations in kidney tubular cells, it is considered as one of the most interesting biomarkers of AKI.[32] Our results extend the repertoire of this biomarker by showing that LCN2 is also induced by chronic ER stress caused by the toxic accumulation of mutant UMOD in TAL cells. The *Umod*^{R186S} kidneys show an early inflammatory response, including upregulation of *Lcn2*, *Lgals3*, or *Cxcl10*,[11] which are all involved in NF-κB signaling and inflammatory responses.[17,33,34] The link between ER stress, tubular damage, and inflammation through NF-κB signaling is well established. NF-κB can be induced by the PERK-ATF4 and IRE1 branches of UPR,[35] which are activated by UMOD aggregates in *Umod*^{R186S} kidneys.[11] The link between LCN2 induction, ER stress, and UPR activation has been demonstrated in a mouse model of proteinuria.[22] Our findings indicated that pharmacological induction of ER stress is in fact sufficient to trigger LCN2 upregulation in tubular cells.

Increased levels of LNC2 have been reported in aggressive subtypes of cancer, associated with increased cell proliferation, cell invasion, and metastasis.[36] In addition, LCN2 has been shown to be an active player in CKD progression in mouse models of nephron reduction, juvenile cystic kidney, and proteinuria.[22,23] The genetic deletion of LCN2 in these different models decreased the severity of tubular lesions and improved the kidney phenotype. By contrast, our data indicated that the deletion of LCN2 does not affect the phenotype or any structural damage in kidneys of the *Umod*$^{R186S/+}$ mice. The disease is progressing similarly over time, in the presence or absence of LCN2. These results are surprising considering the massive upregulation of LCN2 in the *Umod*$^{R186S/+}$ kidneys and the protection observed in the mouse models of nephron reduction and proteinuric damage.[22,23] An important factor could be that the two latter mouse models were on the FVB/*N* background, particularly sensitive to kidney damage, whereas the *Umod*$^{R186S/+}$ mice are on the C57BL/6.[22,23] A strain effect could explain why similar UPR and LCN2 induction in proteinuric mouse model and *Umod*$^{R186S/+}$ mouse model led to different outcomes. In the former, this induction results in apoptosis and tubulointerstitial damage, which significantly improved after LCN2 deletion, while in the latter, LCN2 deletion had no beneficial effect, and the damage was not accompanied by apoptosis.[11,22] The nephron segment affected in each model could also contribute to the observed discrepancies. The *Umod*^{R186S} model primarily targets TAL, whereas the proteinuric models involve broader tubular injury including the proximal tubules. Because LCN2 is expressed and responsive in proximal tubule cells, its pathogenic role may be more prominent when this segment is involved. These findings suggest that LCN2 induction is a biomarker of tubular ER stress, but not a mediator of kidney damage in the *Umod*$^{R186S/+}$ mouse model of ADTKD.

Iron accumulation is common in CKD, with iron deposits thought to result from leakage of transferrin-bound iron, leading to abnormal reabsorption by proximal tubules and increased iron exposure in distal tubules. Iron deposition is also associated with dysregulation of iron importers/exporters and iron storage proteins.[37] We observed a global increase in iron load in the *Umod*$^{R186S/+}$ kidneys, affecting both tubular and interstitial compartments, predominantly near TAL cells where mutant UMOD accumulates. The relationship between iron accumulation and interstitial fibrosis in CKD remains unclear.

Administration of an iron chelator, deferasirox, in rat and mouse models of CKD attenuated fibrosis by inhibiting oxidative stress and TGF-β signaling.[38,39] Conversely, the chelator desferrioxamine was shown to exacerbate kidney lesions in FVB/*N* mice after nephron reduction, linked to an increase in LCN2 expression.[23] Our data showed that the iron load is significantly decreased in *Umod*$^{R186S/+}$; *Lcn2*$^{-/-}$ mice, supporting that LCN2 contributes to iron accumulation in mutant kidneys. Apart from reduction in total iron, the deletion of LCN2 was only reflected by subtle changes in *Umod*$^{R186S/+}$ kidneys, including upregulation of *Slc40a1* and downregulation of *Tfrc*, with no proferroptotic phenotype.

Increased levels of LCN2 were suggested to contribute to dysregulated iron metabolism in *Col4a3*^{KO} mouse model of CKD[40] and in proteotoxic stress in neurodegenerative diseases. LCN2 upregulation has been reported in the frontal cortex of patients with Alzheimer's disease, with serum LCN2 levels positively correlating with white matter changes.[41] In a mouse model of Alzheimer's disease induced by injection of amyloid-beta oligomers, increased LCN2 expression was accompanied by iron dysregulation.[41] In the J20 Alzheimer's disease mouse model, deletion of *Lcn2* reduced brain iron accumulation but did not alter the progression of the Alzheimer's disease–like phenotype.[42] These parallels between Alzheimer's disease and ADTKD-*UMOD* highlight a potentially conserved role for LCN2 as a biomarker of proteotoxic stress, with a context-dependent contribution to disease progression.

In conclusion, LCN2 is strongly induced by mutant UMOD aggregates in TAL cells, extending its repertoire as a biomarker of ER stress and toxic proteinopathy. The deletion of LCN2 reduced iron accumulation in the kidney but did not alter key damage pathways, structural kidney changes, or disease progression in the *Umod*$^{R186S/+}$ mouse model of ADTKD-*UMOD*.

Disclosures

Disclosure forms, as provided by each author, are available with the online version of the article at http://links.lww.com/JSN/F768.

Author Contributions

Conceptualization: Olivier Devuyst, Jennifer Lake, Fabiola Terzi.
Formal analysis: Qin Guo, Jennifer Lake, Holly Mabillard, Marta Mariniello, Eric Olinger, John A. Sayer, Guglielmo Schiano.
Funding acquisition: Olivier Devuyst.
Investigation: Qin Guo, Jennifer Lake, Marta Mariniello, Eric Olinger, Guglielmo Schiano, Fabiola Terzi.
Resources: Fabiola Terzi.
Supervision: Olivier Devuyst.
Writing – original draft: Olivier Devuyst, Jennifer Lake, Fabiola Terzi.
Writing – review & editing: Olivier Devuyst, Jennifer Lake, Holly Mabillard, Marta Mariniello, Eric Olinger, John A. Sayer, Guglielmo Schiano, Fabiola Terzi.

Funding

O. Devuyst: Schweizerischer Nationalfonds zur Förderung der Wissenschaftlichen Forschung, Universität Zürich, ERA-NET, and EJP 2023.

Acknowledgments

Marta Mariniello and Olivier Devuyst are supported by the European Union's Horizon 2020 research and innovation program under the Marie Skłodowska-Curie grant (agreement N° 860977). Olivier Devuyst is supported by the European Reference Network for Rare Kidney Diseases (project N° 739532), the Swiss National Science Foundation (grant 10.003.608), and the University Research Priority Program (URPP) ITINERARE at the University of Zurich. Eric Olinger is supported by Postdoc Mobility-Stipendien of the Swiss National Science Foundation Grants P2ZHP3_195181 and P500PB_206851, and Kidney Research UK Grant Paed_RP_001_20180925. Fabiola Terzi is supported by Institut National de la Santé et de la Recherche Médicale, Université de Paris Cité, Agence Nationale Recherche. Holly Mabillard is a Medical Research Council Clinical Doctoral Training Fellow (MR/V028723/1). John A. Sayer is supported by Kidney Research UK (24/01), Northern Counties Kidney Research Fund (Paed_RP_001_20180925, RP_007_20210729), and the Medical Research Council (MR/Y007808/1). We thank Aleksandra Kokanovic, Nadine Nägele, and Sara Botta for expert technical assistance. The *Umod*^{C125R} line was developed and kindly provided by Prof. Rajesh V. Thakker (Academic Endocrine Unit, Radcliffe Department of Medicine, University of Oxford, Oxford, United Kingdom). Two of the authors of this publication are members of the European Reference Network for Rare Kidney Diseases (ERKNet): Olivier Devuyst and Eric Olinger. Eric Olinger is board member of the Genes & Kidney working group of the European Renal Association.

Declarative Statements

This study includes clinical experimentation and received Institutional Review Board or Ethics Committee approval. All patients provided written informed consent. All animal experiments were conducted in accordance with the NIH Guide for the Care and Use of Laboratory Animals or an equivalent standard that meets or exceeds the ethical and welfare requirements outlined in the NIH Guide. All protocols were approved by the appropriate institutional animal care and use committee.

Data Availability Statements

All original data, including deidentified patient-level data or individual laboratory data measurements, are included in the manuscript and/or supplemental material. Data Type: Raw Data/Source Data; Observational Data. Original data generated for the study will be made available upon reasonable request to the corresponding author. Primary RNA-sequencing data are available on Gene Expression Omnibus (accession number: GSE214491).

Supplemental Material

This article contains supplemental material online, published as provided by the authors, at http://links.lww.com/JSN/F769, http://links.lww.com/JSN/F770.

Supplemental Methods.

Supplemental Figure 1. LCN2 expression and localization in *Umod*$^{R186S/+}$ mice.

Supplemental Figure 2. Upregulation of stress response pathways associated with LCN2 induction in *Umod* KI mice.

Supplemental Figure 3. *UMOD* variants and corresponding urinary LCN2 levels in patients with ADTKD-*UMOD*.

Supplemental Figure 4. Thapsigargin treatment increases LCN2 expression in *UMOD* WT cells.

Supplemental Figure 5. Torin1 treatment decreases LCN2 expression in *UMOD* C170Y cells.

Supplemental Figure 6. Early induction of inflammation in *Umod*$^{R186S/+}$; *Lcn2* mice.
Supplemental Figure 7. Iron dysregulation in *Umod*$^{R186S/+}$ mice.
Supplemental Figure 8. Uncropped Western blot membranes.
Supplemental Table 1. Clinical characteristics of patients with ADTKD-*UMOD* and healthy controls.
Supplemental Table 2. *UMOD* variants and corresponding urinary LCN2 levels in patients with ADTKD-*UMOD*.
Supplemental Table 3. Primers used for real-time RT-PCR analysis.
Supplemental Table 4. List of antibodies.
Source data (Excel).

References

1. Devuyst O, Olinger E, Weber S, et al. Autosomal dominant tubulointerstitial kidney disease. *Nat Rev Dis Primers.* 2019;5(1):60. doi:10.1038/s41572-019-0109-9
2. Groopman EE, Marasa M, Cameron-Christie S, et al. Diagnostic utility of exome sequencing for kidney disease. *N Engl J Med.* 2019;380(2):142–151. doi:10.1056/NEJMoa1806891
3. Schaeffer C, Devuyst O, Rampoldi L. Uromodulin: roles in health and disease. *Annu Rev Physiol.* 2021;83:477–501. doi:10.1146/annurev-physiol-031620-092817
4. Dahan K, Devuyst O, Smaers M, et al. A cluster of mutations in the UMOD gene causes familial juvenile hyperuricemic nephropathy with abnormal expression of uromodulin. *J Am Soc Nephrol.* 2003;14(11):2883–2893. doi:10.1097/01.ASN.0000092147.83480.b5
5. Olinger E, Schaeffer C, Kidd K, et al. An intermediate-effect size variant in UMOD confers risk for chronic kidney disease. *Proc Natl Acad Sci U S A.* 2022;119(33):e2114734119. doi:10.1073/pnas.2114734119
6. Bernascone I, Janas S, Ikehata M, et al. A transgenic mouse model for uromodulin-associated kidney diseases shows specific tubulo-interstitial damage, urinary concentrating defect and renal failure. *Hum Mol Genet.* 2010;19(15):2998–3010. doi:10.1093/hmg/ddq205
7. Johnson BG, Dang LT, Marsh G, et al. Uromodulin p.Cys147Trp mutation drives kidney disease by activating ER stress and apoptosis. *J Clin Invest.* 2017;127(11):3954–3969. doi:10.1172/JCI93817
8. Kemter E, Rathkolb B, Rozman J, et al. Novel missense mutation of uromodulin in mice causes renal dysfunction with alterations in urea handling, energy, and bone metabolism. *Am J Physiol Renal Physiol.* 2009;297(5):F1391–F1398. doi:10.1152/ajprenal.00261.2009
9. Kemter E, Prueckl P, Sklenak S, et al. Type of uromodulin mutation and allelic status influence onset and severity of uromodulin-associated kidney disease in mice. *Hum Mol Genet.* 2013;22(20):4148–4163. doi:10.1093/hmg/ddt263
10. Piret SE, Olinger E, Reed AAC, et al. A mouse model for inherited renal fibrosis associated with endoplasmic reticulum stress. *Dis Model Mech.* 2017;10(6):773–786. doi:10.1242/dmm.029488
11. Schiano G, Lake J, Mariniello M, et al. Allelic effects on uromodulin aggregates drive autosomal dominant tubulointerstitial kidney disease. *EMBO Mol Med.* 2023;15(12):e18242. doi:10.15252/emmm.202318242
12. Xiao X, Yeoh BS, Vijay-Kumar M. Lipocalin 2: an emerging player in iron homeostasis and inflammation. *Annu Rev Nutr.* 2017;37:103–130. doi:10.1146/annurev-nutr-071816-064559
13. Liu Q, Nilsen-Hamilton M. Identification of a new acute phase protein. *J Biol Chem.* 1995;270(38):22565–22570. doi:10.1074/jbc.270.38.22565
14. Goetz DH, Holmes MA, Borregaard N, Bluhm ME, Raymond KN, Strong RK. The neutrophil lipocalin NGAL is a bacteriostatic agent that interferes with siderophore-mediated iron acquisition. *Mol Cell.* 2002;10(5):1033–1043. doi:10.1016/s1097-2765(02)00708-6
15. Bao G, Clifton M, Hoette TM, et al. Iron traffics in circulation bound to a siderocalin (Ngal)-catechol complex. *Nat Chem Biol.* 2010;6(8):602–609. doi:10.1038/nchembio.402
16. Devireddy LR, Gazin C, Zhu X, Green MR. A cell-surface receptor for lipocalin 24p3 selectively mediates apoptosis and iron uptake. *Cell.* 2005;123(7):1293–1305. doi:10.1016/j.cell.2005.10.027
17. Buonafine M, Martinez-Martinez E, Jaisser F. More than a simple biomarker: the role of NGAL in cardiovascular and renal diseases. *Clin Sci.* 2018;132(9):909–923. doi:10.1042/CS20171592
18. Singer E, Markó L, Paragas N, et al. Neutrophil gelatinase-associated lipocalin: pathophysiology and clinical applications. *Acta Physiol.* 2013;207(4):663–672. doi:10.1111/apha.12054
19. Shlipak MG, Day EC. Biomarkers for incident CKD: a new framework for interpreting the literature. *Nat Rev Nephrol.* 2013;9(8):478–483. doi:10.1038/nrneph.2013.108
20. Mishra J, Mori K, Ma Q, et al. Amelioration of ischemic acute renal injury by neutrophil gelatinase-associated lipocalin. *J Am Soc Nephrol.* 2004;15(12):3073–3082. doi:10.1097/01.ASN.0000145013.44578.45
21. Mori K, Lee HT, Rapoport D, et al. Endocytic delivery of lipocalin-siderophore-iron complex rescues the kidney from ischemia-reperfusion injury. *J Clin Invest.* 2005;115(3):610–621. doi:10.1172/JCI23056
22. El Karoui K, Viau A, Dellis O, et al. Endoplasmic reticulum stress drives proteinuria-induced kidney lesions via lipocalin 2. *Nat Commun.* 2016;7:10330. doi:10.1038/ncomms10330
23. Viau A, El Karoui K, Laouari D, et al. Lipocalin 2 is essential for chronic kidney disease progression in mice and humans. *J Clin Invest.* 2010;120(11):4065–4076. doi:10.1172/JCI42004
24. Berger T, Togawa A, Duncan GS, et al. Lipocalin 2-deficient mice exhibit increased sensitivity to Escherichia coli infection but not to ischemia-reperfusion injury. *Proc Natl Acad Sci U S A.* 2006;103(6):1834–1839. doi:10.1073/pnas.0510847103
25. Joseph CB, Mariniello M, Yoshifuji A, et al. Meta-GWAS reveals novel genetic variants associated with urinary excretion of uromodulin. *J Am Soc Nephrol.* 2022;33(3):511–529. doi:10.1681/ASN.2021040491
26. Ewald JD, Zhou G, Lu Y, et al. Web-based multi-omics integration using the analyst software suite. *Nat Protoc.* 2024;19(5):1467–1497. doi:10.1038/s41596-023-00950-4
27. Chen D, Fan Z, Rauh M, Buchfelder M, Eyupoglu IY, Savaskan N. ATF4 promotes angiogenesis and neuronal cell death and confers ferroptosis in a xCT-dependent manner. *Oncogene.* 2017;36(40):5593–5608. doi:10.1038/onc.2017.146
28. Liu J, Song X, Kuang F, et al. NUPR1 is a critical repressor of ferroptosis. *Nat Commun.* 2021;12(1):647. doi:10.1038/s41467-021-20904-2
29. Zhu S, Zhang Q, Sun X, et al. HSPA5 regulates ferroptotic cell death in cancer cells. *Cancer Res.* 2017;77(8):2064–2077. doi:10.1158/0008-5472.CAN-16-1979
30. Kuang F, Liu J, Tang D, Kang R. Oxidative damage and antioxidant defense in ferroptosis. *Front Cell Dev Biol.* 2020;8:586578. doi:10.3389/fcell.2020.586578. https://www.frontiersin.org/articles/10.3389/fcell.2020.586578.
31. Marques E, Teixeira MA, Nguyen C, Terzi F, Gallazzini M. Lipocalin-2 induces mitochondrial dysfunction in renal tubular cells via mTOR pathway activation. *Cell Rep.* 2023;42(9)113032. doi:10.1016/j.celrep.2023.113032
32. Abella V, Scotece M, Conde J, et al. The potential of lipocalin-2/NGAL as biomarker for inflammatory and metabolic diseases. *Biomarkers.* 2015;20(8):565–571. doi:10.3109/1354750X.2015.1123354
33. Yeruva S, Ramadori G, Raddatz D. NF-κB-dependent synergistic regulation of CXCL10 gene expression by IL-1β and IFN-γ in human intestinal epithelial cell lines. *Int J Colorectal Dis.* 2008;23(3):305–317. doi:10.1007/s00384-007-0396-6
34. Zhou W, Chen X, Hu Q, Chen X, Chen Y, Huang L. Galectin-3 activates TLR4/NF-κB signaling to promote lung adenocarcinoma cell proliferation through activating lncRNA-NEAT1 expression. *BMC Cancer.* 2018;18(1):580. doi:10.1186/s12885-018-4461-z
35. Gallazzini M, Pallet N. Endoplasmic reticulum stress and kidney dysfunction. *Biol Cell.* 2018;110(9):205–216. doi:10.1111/boc.201800019
36. Santiago-Sánchez GS, Pita-Grisanti V, Quiñones-Díaz B, Gumpper K, Cruz-Monserrate Z, Vivas-Mejía PE. Biological

functions and therapeutic potential of lipocalin 2 in cancer. *Int J Mol Sci*. 2020;21(12):E4365. doi:10.3390/ijms21124365
37. van Raaij S, van Swelm R, Bouman K, et al. Tubular iron deposition and iron handling proteins in human healthy kidney and chronic kidney disease. *Sci Rep*. 2018;8(1):9353. doi:10.1038/s41598-018-27107-8
38. Ikeda Y, Ozono I, Tajima S, et al. Iron chelation by deferoxamine prevents renal interstitial fibrosis in mice with unilateral ureteral obstruction. *PLoS One*. 2014;9(2):e89355. doi:10.1371/journal.pone.0089355
39. Naito Y, Fujii A, Sawada H, et al. Association between renal iron accumulation and renal interstitial fibrosis in a rat model of chronic kidney disease. *Hypertens Res*. 2015;38(7):463–470. doi:10.1038/hr.2015.14
40. Courbon G, Francis C, Gerber C, et al. Lipocalin 2 stimulates bone fibroblast growth factor 23 production in chronic kidney disease. *Bone Res*. 2021;9(1):35. doi:10.1038/s41413-021-00154-0
41. Kang H, Shin HJ, An HS, et al. Role of Lipocalin-2 in amyloid-beta oligomer-induced mouse model of Alzheimer's disease. *Antioxidants*. 2021;10(11):1657. doi:10.3390/antiox10111657
42. Dekens DW, Naudé PJW, Keijser JN, Boerema AS, De Deyn PP, Eisel ULM. Lipocalin 2 contributes to brain iron dysregulation but does not affect cognition, plaque load, and glial activation in the J20 Alzheimer mouse model. *J Neuroinflammation*. 2018;15(1):330. doi:10.1186/s12974-018-1372-5